In vivo time-resolved sub-pixel measurements of wall deformation in the common carotid artery

Stéphane Avril, Fabien Schneider, Chrisitan Boissier

In vivo time-resolved sub-pixel measurements of wall deformation in the common carotid artery

Stéphane Avril[(1)], Fabien Schneider[(2)], Christian Boissier[(3)]

[(1)] Center for Health Engineering
Ecole Nationale Supérieure des Mines de Saint-Étienne
PECM - CNRS UMR 5146 ; IFRESIS - INSERM IFR 143
158 Cours Fauriel, 42023 SAINT-ÉTIENNE cedex 2, FRANCE

[(2)] Radiologie Centrale hôpital nord
CHU de Saint Etienne
42055 SAINT-ÉTIENNE cedex 2, FRANCE

[(3)] Médecine Vasculaire hôpital nord
CHU de Saint Etienne
42055 SAINT-ÉTIENNE cedex 2, FRANCE

Abstract

In this paper, we present a new approach for time-resolved measurements of wall deformation in human arteries using MRI and we prove its feasibility on an example. The purpose of the approach is to derive the local elastic properties of the carotid artery. Repeatable results obtained on two volunteers point out the promising potential of this approach for investigating the mechanics of arterial tissues *in vivo*.

1 Introduction

It is well assessed that, despite biochemical and hemodynamical factors play a primary role in the development of most vascular disorders, solid mechanics models may contribute to understand their genesis and progression. The realism of models in solid mechanics depends significantly on the mechanical properties used as input parameters. Therefore, characterizing the biomechanical properties of arteries remains an essential issue. Recent advances demonstrate that geometric and material parameters can be identified from *in vivo* human data [1,2], which enables computations of *in vivo* wall stresses using methods of nonlinear mechanics. However, the main requirement to this is measuring the deformation of the vessel wall *in vivo*.

In vivo quantification of vessel wall cyclic strain has also important applications in physiology and disease research and the design of intravascular devices. Better understanding of both normal and abnormal wall motion and strain distributions will contribute to a better understanding of disease processes as well as potentially aid in the characterization of vulnerable plaques and aneurysms; for example, changes in wall motion and strain patterns may help predicting which plaque are more likely to enlarge rapidly and/or rupture.

Various ultrasound techniques have been used to detect and track the vessel wall motion. Computational

techniques have mainly been based on analysis of the B-mode greyscale images [3,4], M-mode [5], analyses of the raw RF ultrasound data [6], echotracking technique [7] and Doppler techniques [8]. However, ultrasounds were only used for imaging longitudinal cross sections of arteries. Imaging cross sections perpendicular to the vessel was achieved with Intravascular Ultrasound (IVUS) [9], but IVUS is a rather intrusive method.

Magnetic Resonance Imaging (MRI) may be a non-intrusive technique well suited to the measurement of artery deformation in the cross section plane perpendicular to the vessel. MRI was often employed to imaging of artery shape and composition [10], but much less often to measure artery deformation [11]. Time-dependent magnetic resonance (MR) magnitude images acquired perpendicular to a given vessel can be used to track the luminal boundary of the vessel over time, and the displacement of this boundary can be used to approximate cyclic strain based on the change in radius of the vessel [12]. This method has several artifacts that can produce errors in determining the boundary of the lumen, which in turn lead to errors in computed strain. An alternate method, MR tagging [13] directly acquires displacement data. However, this method requires the pixel size to be small compared to the organ spatial dimensions, displacements, and heterogeneity of the strain field being studied. Current MR spatial resolution is not adequate to measure displacement and strain accurately in vessel walls using this method. A third MR-based method for quantifying motion and strain utilizes MR phase contrast (PC) velocity data. This method was presented as the basis of the approach to non-invasively measure vessel wall strain *in vivo* [14]. However, difficulties arise in setting the appropriate sensitivity (trade-off between unwrapping difficulties and low signal to noise ratio). Moreover, slight angles between the artery axis and the imaging plane induce a sensitivity to the out-of-plane velocity, which is the blood velocity, ten times larger, hence overwhelming the signal coming from wall deformation. Eventually, this technique requires that the voxel size is at least twice smaller than the thickness of the artery wall, which is still not reachable for thin arteries such as the healthy carotid artery.

In summary, the state of the art for measuring the cross-sectional deformation of arteries using MRI is:

1. either measuring deformation or strains in the thickness of arteries (PC-MRI, tagging) but this is only feasible for thick arteries given that the smallest reachable pixel size in clinical conditions is around 0.4 mm;

2. or tracking the luminal boundary of the vessel over time but this can only be accurate using subpixel techniques for tracking the wall.

This study is aimed at addressing the deformation of the common carotid artery (CCA) because the carotid artery is a useful window for cardiovascular risk. As it is not possible to increase easily the spatial resolution of MRI, it was decided to work on the second point: subpixel tracking. More specifically, it will be shown

that subpixel tracking can be achieved using optical flow on PC-MRI magnitude image. Eventually, the obtained deformation is used to derive the elastic properties of the carotid artery. Applications on real human data are shown for the sake of feasibility proof.

2 Materials and Methods

2.1 Origin of clinical data

All subjects signed an informed consent. MRI data and blood pressure were recorded successively following 15 min of recumbent rest in a room dedicated to echography. Data used herein are from two healthy subjects: a 23-year-old man (patient A) and a 26-year-old man (patient B).

2.2 Obtaining magnitude images throughout the cardiac cycle

Phase contrast MR angiography has sometimes been used to quantify flow velocity [15]. Let us recall the principles of this sequence. The flow is encoded in the phase rather than the magnitude of the MRI signal. Between Radio-Frequency (RF) excitation and imaging, velocity encoding is performed by applying two equal and opposite gradients with a short delay between them. If the material within a voxel is stationary, then the phase shift caused by one gradient will be canceled by the equal and opposite phase shift due to the other, and the net phase change measured will be zero. However, if material moves along the direction of the gradient, then it will gain a net phase shift proportional to this component of velocity.

Blood and the surrounding tissues also have distinct T_1 and T_2 relaxation parameters, giving clear contrast in the magnitude images in the sequence [16]. We used this to estimate the location of the artery contour and its deformations.

Although it is also possible to estimate the location of the artery contour from the phase images, we found that in the magnitude images the gradient at the vessel wall was higher and independent of blood flow. Moreover, the signal outside the artery was less noisy for the magnitude images, enhancing contour estimation.

The scanner used in our study was a 3T Siemens Tim Trio system (IRMAS, Saint-Etienne, France). A 2D spin-echo FLASH sequence was used to acquire a single 3 mm thick slice of a lying volunteer's neck with a matrix size of 256×256 giving in-plane dimensions 0.39×0.39 mm^2. A cine sequence, with one segment per cycle was used to acquire the temporal evolution of the flow throughout the pulse. Heart beats were detected by the measurement of blood flow in a patient's finger with near infrared spectrometry. The cine data were reconstructed to give 42 snapshots evenly distributed throughout the cardiac cycle, corresponding to a mean sampling frequency of 61.5 s^{-1} (T=0.81s). The repetition time was TR=64 ms and the echo time was TE=5.4 ms.

The magnitude of the signal was digitized with a 16 bits resolution (integer numbers between 0 and 65535).

Eventually, the magnitude image is a 3D array of size 256×256×42, denoted $\widetilde{I}(x_p, y_q, t_n)$, for p varying from 1 to 256, q varying from 1 to 256 and n varying from 1 to 42. Actually, the same magnitude images were achieved at 3 different cross sections of the neck separated by 24 mm. One cross section was before the carotid bifurcation in the CCA, one at the bifurcation and the third one after the bifurcation. Only the cross section of the CCA will be considered further.

2.3 Determining the curve of the vessel wall average location

The magnitude of the signal is well suited for determining the edges of the artery because, due to the large quantity of blood flowing in the artery and also due to the distinct T_1 and T_2 relaxation parameters between blood and the surrounding tissues, the magnitude of the signal is larger inside the artery than outside.

Let (x_0, y_0) be the average location of the center of gravity of the artery in the imaging plane over a cardiac cycle. Let us define the closed curve around (x_0, y_0) figuring all the points belonging to the vessel wall. The thickness of the vessel wall is neglected as it is approximately similar to the pixel size in the images. This justifies to represent the cross section of the vessel wall by a closed curve. This curve is denoted $\mathfrak{C}(t)$, where t denotes time. The curve changes its shape and size over time due to the varying blood pressure. The curve is defined in a polar way, such as $(x(t), y(t))$ belongs to this curve if:

$$\begin{cases} x(t) = x_0 + r(\theta, t)\cos(\theta) \\ y(t) = y_0 + r(\theta, t)\sin(\theta) \\ 0 \leq \theta \leq 2\pi \end{cases} \tag{1}$$

with a Fourier decomposition of $r(\theta, t)$ up to order N:

$$r(\theta, t) = \sum_{k=0}^{N} [a_k(t)\cos(k\theta) + b_k(t)\sin(k\theta)] \tag{2}$$

Let $\bar{a}_k$ and $\bar{b}_k$ denote respectively the average value of $a_k(t)$ and $b_k(t)$ over a period T (cardiac cycle = time between two heart beats).

The values of $\bar{a}_k$ and $\bar{b}_k$ are determined like this:

1. $\widetilde{I}(x_p, y_q, t_n)$ is averaged over time in order to deduce the average intensity $\bar{I}(x_p, y_q)$ at each voxel:

$$\bar{I}(x_p, y_q) = \frac{1}{42} \sum_{n=1}^{42} \widetilde{I}(x_p, y_q, t_n) \tag{3}$$

2. the gradient of the average intensity $\nabla\bar{I}(x_p, y_q)$ is deduced like this:

$$\nabla\bar{I}(x_p, y_q) = \frac{1}{2}\sqrt{[\bar{I}(x_{p+1}, y_q) - \bar{I}(x_{p-1}, y_q)]^2 + [\bar{I}(x_p, y_{q+1}) - \bar{I}(x_p, y_{q-1})]^2} \tag{4}$$

The formula in Eq. 4 is not valid for the edges of the image but this does not concern the carotids which are sufficiently far from the edges so gradients on the edges are disregarded.

The obtained images of $\nabla\bar{I}$ show the largest gradients at the location of the artery wall (Fig. 4).

3. Pixels belonging to the vessel wall are tracked as the pixels having the largest values in $\nabla\bar{I}$. An algorithm based on the watershed theory [17] was developed for this. However it can fail sometimes so a possibility of selecting manually some points belonging to the arterial wall on the $\nabla\bar{I}$ was implemented. Let $(\tilde{x}_i, \tilde{y}_i)$ be the coordinates of the selected points (manually or using the watershed algorithm).

4. Least squares regression is achieved. It consists in finding the coefficients $\bar{a}_k$ and $\bar{b}_k$ that minimize the following cost function:

$$J = \sum_i \left[\sum_{k=0}^{N} \left[\bar{a}_k \cos(k\tilde{\theta}_i) + \bar{b}_k \sin(k\tilde{\theta}_i) \right] - \tilde{r}_i \right]^2 \tag{5}$$

where:

$$\begin{array}{l} \tilde{r}_i = \sqrt{(\tilde{x}_i - x_0)^2 + (\tilde{y}_i - x_0)^2} \\ \tilde{\theta}_i = \arg((\tilde{x}_i - x_0) + j\,(\tilde{y}_i - y_0)) \\ j^2 = -1 \end{array} \tag{6}$$

Let $\overline{\mathfrak{C}}$ be the curve of polar expression:

$$r(\theta) = \sum_{k=0}^{N} \left[\bar{a}_k \cos(k\theta) + \bar{b}_k \sin(k\theta) \right] \tag{7}$$

$\overline{\mathfrak{C}}$ defines the average shape of the artery over the cardiac cycle.

Eventually, the curve defining the artery wall is supposed to satisfy the following polar equation:

$$r(\theta,t) = \sum_{k=0}^{N} \left[\bar{a}_k \cos(k\theta) + \bar{b}_k \sin(k\theta) \right] + \sum_{k=0}^{N} \frac{p(t) - p_0}{\alpha_k} \cos(k\theta) + \frac{p(t) - p_0}{\beta_k} \sin(k\theta) \tag{8}$$

where $p(t)$ is the intraluminal pressure at time t, p_0 is its average over a period T. The coefficients α_k and β_k are related to the geometric and stiffness properties of the artery and its surrounding medium. Complex numbers may be used instead of real numbers for taking into account the viscoelastic properties of the artery and its surrounding medium. In this case, α_k and β_k, and consequently $r(\theta,t)$, would be complex numbers instead of real numbers. However, the viscoelastic properties will be discussed in a future study.

2.4 Pressure measurements by applanation tonometry

The intraluminal pressure applied by the blood is assumed constant across any slice of the artery, only depending on t.

Right intraluminal CCA pressure waveforms were recorded non-invasively for 9s at 128Hz with a pressure tonometer (Sphygmocor, AtCor Medical).

A system for noninvasively and continuously monitoring arterial blood pressure includes a tissue stress sensor. The sensor has a continuous diaphragm for sensing stress within tissue near a preselected artery, the stress being caused by arterial pulsations within that artery. The stress sensitive diaphragm is coupled with electromechanical means for producing electrical signals that represent the stress within the tissue that is communicated to the sensor. These signals are then processed electronically in order to yield an output that is indicative of the arterial blood pressure of the preselected artery. The disclosed system includes methods of operation for determining blood pressure while maintaining a preselected artery in an optimum applanation state and an off-optimum applanation state.

2.5 Processing the magnitude images for determining the curve of the vessel wall over time

The objective now is to obtain α_k and β_k defined in Eq. 13, for $k = 0$ to N. For this, a set of 30 points evenly distributed along the $\overline{\mathfrak{C}}$ curve are defined. Their cartesian coordinates are denoted $(\bar{x}_m, \bar{y}_m)$ and their polar coordinates $(\bar{r}_m, \bar{\theta}_m)$, with $1 \leq m \leq 30$. For any of these points, their position will change over time due to pressure variations. Let $(x_m(t), y_m(t))$ denote their location in cartesian coordinates at any time t and $(r_m(t), \theta_m(t))$ in polar coordinates. It is assumed that the motion due to the pressure variations satisfies the following rule:

$$\begin{cases} \dot{x}_m = \frac{dx_m}{dt} = \frac{dr_m}{dt}\cos(\bar{\theta}_m) \\ \dot{y}_m = \frac{dy_m}{dt} = \frac{dr_m}{dt}\sin(\bar{\theta}_m) \end{cases} \tag{9}$$

which means that we neglect the velocity component perpendicular to the radial direction, hence $\theta_m(t) = \bar{\theta}_m$.

If $I(x,y,t)$ denotes a continuous representation of the magnitude of the MRI signal over time and space, the conservation of the magnitude (theory of optical flow [18]) yields:

$$\dot{x}_m \frac{\partial I}{\partial x}(x_m, y_m) + \dot{y}_m \frac{\partial I}{\partial y}(x_m, y_m) + \frac{\partial I}{\partial t}(x_m, y_m) = 0 \tag{10}$$

Using Eq. 9, we get:

$$\frac{dr_m}{dt} = \frac{-\frac{\partial I}{\partial t}(x_m, y_m)}{\cos(\bar{\theta}_m)\frac{\partial I}{\partial x}(x_m, y_m) + \sin(\bar{\theta}_m)\frac{\partial I}{\partial y}(x_m, y_m)} \tag{11}$$

From Eq. 13, it may be written:

$$\frac{dr_m}{dt} = \frac{dp}{dt}\sum_{k=0}^{N}\left[\frac{\cos(k\bar{\theta}_m)}{\alpha_k} + \frac{\sin(k\bar{\theta}_m)}{\beta_k}\right] \tag{12}$$

Eventually, it means that α_k and β_k must satisfy the following equations, for $1 \leq m \leq 30$:

$$\frac{dp}{dt}\sum_{k=0}^{N}\left[\frac{\cos(k\bar{\theta}_m)}{\alpha_k}+\frac{\sin(k\bar{\theta}_m)}{\beta_k}\right]=\frac{-\frac{\partial I}{\partial t}(x_m,y_m,t)}{\cos(\bar{\theta}_m)\frac{\partial I}{\partial x}(x_m,y_m,t)+\sin(\bar{\theta}_m)\frac{\partial I}{\partial y}(x_m,y_m),t} \tag{13}$$

To derive the previous equation, we have to deduce a continuous field $I(x,y,t)$ from a discrete number of data points $\widetilde{I}(x_p,y_q,t_n)$. Diffuse Approximation (DA) has proved to be a very efficient method [19]. DA is based on the Shepard's interpolation method [20] which defines $I(x,y,t)$ such as:

$$I(x,y,t)=\sum_p\sum_q\sum_n W_x(x-x_p)W_y(y-y_p)W_t(t-t_n)\widetilde{I}(x_p,y_q,t_n) \tag{14}$$

where:

$$\begin{aligned}
W_x(x-x_p)&=\frac{\exp(-(x-x_p)^2/R_x^2)}{256\times 42\times\sum_{p=1}^{256}\exp(-(x-x_p)^2/R_x^2)}\\
W_y(y-y_q)&=\frac{\exp(-(y-y_q)^2/R_y^2)}{256\times 42\times\sum_{q=1}^{256}\exp(-(y-y_q)^2/R_y^2)}\\
W_t(t-t_n)&=\frac{\exp(-(t-t_n)^2/R_t^2)+\exp(-[T-(t-t_n)]^2/R_t^2)}{256\times 256\times\sum_{n=1}^{42}\left[\exp(-(t-t_n)^2/R_t^2)+\exp(-[T-(t-t_n)]^2/R_t^2)\right]}
\end{aligned} \tag{15}$$

R_x, R_y and R_t are chosen in order to control the filtering effect in each direction (trade-off between the search of a relevant filtering effect and the risk of spoiling local information). R_x, R_y and R_t are called the sizes of the filtering kernels, as W_x, W_y and W_t may be named "filtering kernels". The choice for R_x and R_y is about the pixel size (the precise value of R_x and R_y may vary from one set of data to another and it will be provided along with the results) which means that the weighting functions act on the few pixels in the neighborhood of (x,y). The choice for R_t is about $T/10$ (the precise value of R_t may vary from one set of data to another and it will be provided along with the results) which means that one of the two exponentials in W_t is always negligible with regard to the others (the presence of both exponentials is for taking into account the periodicity of the signal: signal from the preceding or following period is taken into account in the interpolation/filtering process).

Eq. 14 gives a continuous form of the intensity $I(x,y,t)$. From it, the partial derivatives $\frac{\partial I}{\partial x}(x_m,y_m,t_n)$, $\frac{\partial I}{\partial y}(x_m,y_m,t_n)$ and $\frac{\partial I}{\partial t}(x_m,y_m,t_n)$ can be deduced.

Then it is possible from Eq. 13 to derive the following equation for all n and m:

$$\sum_{k=0}^{N}\left[\frac{\cos(k\bar{\theta}_m)}{\alpha_k}+\frac{\sin(k\bar{\theta}_m)}{\beta_k}\right]=\frac{-\frac{\partial I}{\partial t}(x_m,y_m,t_n)}{\frac{dp}{dt}(t_n)\left[\cos(\bar{\theta}_m)\frac{\partial I}{\partial x}(x_m,y_m,t_n)+\sin(\bar{\theta}_m)\frac{\partial I}{\partial y}(x_m,y_m,t_n)\right]} \tag{16}$$

A over-determined linear system of equations is obtained in $\frac{1}{\alpha_k}$ and $\frac{1}{\beta_k}$. The resolution is achieved by the linear least-squares method implemented in Matlab [17].

Actually, the problem is not really linear because x_m and y_m, which correspond to the location of the arterial wall at time t_n, must be updated with the values of $\frac{1}{\alpha_k}$ and $\frac{1}{\beta_k}$. In order to address this nonlinearity issue, an iterative algorithm has been implemented. A first resolution using linear least-squares is achieved, taking $x_m = \bar{x}_m$ and $y_m = \bar{y}_m$ in Eq. 16 for starting. Afterwards, the values of x_m and y_m are repeatedly updated by solving again Eq. 16 with the linear least squares method and computing r_m by integrating Eq. 12. The iterations are stopped when solution converges.

2.6 Elastic modulus of the arterial wall

An approximate value of the elastic modulus of the artery can be deduced if the following assumptions are done:

- the pressure outside the artery is zero
- the stress in the arterial wall is uniform and equal to $\sigma(t) = p(t)R_0/h_0$ where $p(t)$ is the intraluminal pressure, R_0 is the average radius and h_0 is average thickness
- the strain in the arterial wall is uniform and equal to $\varepsilon(t) = R(t)/R_0 - 1$, where $R(t)$ is the average radius at t. The average radius is computed as the radius of the disc having the same area as the cross section of the artery.

Then, $E(t) = \sigma(t)/\varepsilon(t)$.

Actually, E is not supposed to depend on time, except if viscoelasticity is considered. Considering only elasticity for this study, the elastic modulus will be deduced as the average of $E(t)$ over time.

2.7 Finite Element modeling

In the previous section, we showed how to derive the location of the vessel wall over time. The obtained curves represent the response of the artery to the systolic and diastolic variations of blood pressure over a heart beat.

It is interesting to verify if a similar response could be retrieved by using a Finite Element (FE) model of the artery and its surrounding tissues.

The model is plane strain. The MRI scan of the neck cross section was segmented and meshed (Fig. 3). Assumptions of infinitesimal strain and linear elasticity are made. Indeed, cyclic strains over a cardiac cycle remain less than 10%, which justifies these assumptions. The CCA is modelled as a membrane with uniform thickness and stiffness.

Viscoelasticity may be discussed but this is beyond the scope of this paper.

In the FE model, the boundary conditions are the inner pressure in the artery. This is a dynamic computation because pressures vary over time. An implicit resolution scheme is adopted. The model takes into account the close jugular vein and all the surrounding soft tissues as a homogeneous soft material. All the neck cross section is modelled, with free edges conditions for the skin. The vertebra lying in the current cross section (C6) is modelled as a clamped rigid solid.

2.8 Measurement of blood flow (optional)

After determining the artery contour throughout the whole heart beat, it is possible to generate a mask to remove all voxels outside it. The mask was applied to the phase maps for investigating the velocity profiles. The velocity encoding gradient was 70 cm/s per π rad in the direction perpendicular to the plane (e.g., head-foot). The phase of the signal was digitized with a 12 bits resolution (integer numbers between 0 and 4295). After unwrapping, the phase was scaled to velocity for all the frames.

3 Results

An example of magnitude image is shown in Fig. 1. It was obtained at a cross section located 24 mm below the carotid bifurcation. A region of interest of 31×31 pixel was selected around the left hand side CCA. The region of interest contains two zones of high intensity (bright zones) which correspond to zones containing blood. They are the internal jugular vein (largest zone) and the left CCA (with a nearly round shape).

The pressure measured by applanation tonometry for the left CCA of this volunteer is shown in Fig. 2. This result is actually the average of the pressure measured over 10 cardiac cycles.

For applying the algorithm based on optical flow to the magnitude images, R_x and R_y were set to value 1.2 and R_t was set to value 2. These values were determined after comparing the results obtained with different filtering parameters (see Fig. 8).

Then, from the magnitude images and the pressure measurements, the average contour of the left CCA was defined and its deformations over time were computed. The maximum and minimum deformations are reported in Fig. 5. It is interesting to notice that the deformation is not a uniform swelling or shrinking all around the artery. The part of the artery which is the farthest from the jugular vein has almost no displacement whereas the part close to the jugular vein moves significantly towards the left. It was noticed that the same effect occurs symmetrically for the right CCA. This means that globally, the displacements are a combination of a translation of the artery towards the jugular vein and of an elastic cyclic shrinking/swelling.

Using the obtained displacements all around the contour of the artery, it was possible to update the contour

all over a cardiac cycle, as shown in Fig. 6. For the 42 frames of this sequence (each frame is represented by a sub-image in Fig. 6), it can be observed that the updated contour is in good agreement with the magnitude image measured at each time step. Actually, the magnitude images may be processed using a segmentation algorithm based on the watershed method [17]. This was achieved and results are shown in Fig. 7. The updated contour obtained with the computed wall displacements is plotted in solid white line whereas the contour deduced directly from the segmentation algorithm is plotted in blue. It can be observed that both contours are globally in agreement. However, the precision of the segmentation algorithm is critical here because of the relatively large pixel size compared to the size of the vessel. Because of that, contours obtained by the segmentation algorithm appear with polygonal shapes, whereas the updated contours have a much more regular shape. Moreover, it must be remembered that the segmentation algorithm failed several times in finding the contours in the magnitude images, because of the poor spatial resolution and because of the proximity with the jugular vein (which has magnitude values similar to the CCA ones). Results shown in Fig. 7 were selected for an example where the segmentation algorithm succeeded to find the contours for all the time frames. However, in practise, a failure rate of about 5 to 10% was observed, as for example in Fig. 9 for the time frames F19 and F20.

The elastic moduli were deduced from the pressure and deformation results. The average thickness was set to $h_0 = 0.5$mm. This value was not measured here but the average value of another study was taken [7]. Measurement of this value by an ultrasound technique is envisaged.

Results were obtained using the two approaches for defining the average contour $\overline{\mathfrak{C}}$. The first approach is to use the watershed segmentation method. This approach gives always the same result from a given MRI scan, which is an advantage. However, the downside is that it can fail to find the contour when the gradient is poor especially in the neighborhood of the jugular vein. This explains why there is no result for the left CCA of V2 in Tab. 1. Results may be obtained systematically by defining the average contour manually. However, the results are user dependent and this may result in large variations of the results, as shown in Tab. 2.

The velocity maps obtained from the MRI data are shown in Fig. 10. The variations of the average velocity over the cardiac cycle is shown in Fig. 11. It can be observed that the velocity and the area have similar forms of variations over the cardiac cycle. Moreover, the time of the largest velocity and the time of the largest cross section area are similar, around 0.65 s.

4 Discussion

4.1 Validation of wall tracking

The optimal choice for R_x and R_y was determined by comparing the radius of the deformed artery computed by the optical flow method to the radius of the artery deduced from the images directly with the watershed segmentation algorithm. The comparison was not possible at all the time frames because the watershed algorithm sometimes failed in tracking the contour. However, for all the time frames for which the contour could be tracked, a value of the radius was derived and compared to the one provided by the optical flow method. The deviation between both radii is shown in Fig. 8 for different values of R_x and R_y. It can be noticed that the deviation is minimized for $R_x = R_y = 1.2$ pixels. This explains why such a value was used for deriving the results reported in Tab. 2.

The optimal choice of R_x and R_y may vary from one scan to another and from one patient to another. An optimal value of 0.6 was found for the other volunteer.

The choice of R_x and R_y was also investigated through the results reported in Tab. 3. It can be noticed that the size of the filtering kernel has a significant impact on the average value. The larger the filtering kernel, the larger the identified modulus. This can be interpreted like this: when the filtering is too large, the sharpness of the local intensity gradient is spread and this tends to underestimate the actual gradient. Consequently, the deformation of the artery is underestimated and this yields an overestimation of the elastic modulus. The correct modulus value can only be deduced thanks to the information provided by Fig. 8.

In Fig. 7 and Fig. 9, the white contour is the contour that has been updated from the average contour with the computed deformation. It is compared to the contour obtained by segmentation. As both contours compare well over the whole cardiac cycle, this means that the deformation obtained from the optical flow approach is in agreement with the raw MRI images.

4.2 Assumption of radial displacements

In Eq. 9, only the radial component of the wall displacements was considered. The component perpendicular to the radial direction was neglected. Actually, results show that this second component is not zero because the there is a rigid body motion of the artery superimposed to the radial displacement induced by the swelling/deflation. As the artery is round, there are locations where the rigid body displacement has only a radial component (in Fig. 5, locations where the magnitudes are minimum and maximum) and locations where the rigid body displacement is perpendicular to the radial direction (at 90° of the previous locations).

Our approach only provides the component of the displacement in the direction of maximum gradient of the

magnitude images. This direction for the artery is the direction perpendicular to the wall, *i.e.* approximately the radial direction, because the magnitude varies maximally when crossing the wall perpendicularly.

However, results shown in Fig. 7 prove that, even if the second component of the displacement is not zero, it remains negligible compared to the radial component. Indeed, by deforming the average contour with only the radial displacement, the contours found by segmentation are recovered. The remaining disagreement between both contours in Fig. 7 may be attributed to the second component of the displacement. Note that this does not affect the estimation of the Young's modulus because its derivation is only based on the changes of radius.

4.3 Sensitivity to the initial contour

It was shown that the definition of the average contour, which is an essential step of the approach, may require that the user selects manually the points on the average magnitude image. This induces variations from one computation to another. These variations are reported in Tab. 2 and Tab. 3. The coefficient of variation (ratio between standard deviation and average) can vary from 4% up to 15%. A correlation was noticed between the sharpness of the gradients at the contours in the gradient images and the coefficient of correlation. When the gradients are sharp, the coefficient of correlation is smaller. This means that the image is less noisy around the artery and that the contour can be tracked with a better repeatability. The sharpness of the gradient is assessed by the failure ratio of the watershed segmentation algorithm. For instance, it was noted that the watershed segmentation algorithm failed with a 90% ratio for the left CCA of V2. This corresponds to the largest coefficient of variation reported in Tab. 2.

4.4 Repeatability

The MRI sequence was repeated a second time on volunteer 1 (V1), providing two independent sets of data for V1. The results in terms of elastic modulus obtained with those two sets are reported in Tab. 4. They show that there is no significant difference between the results obtained with both sets. The difference is within the scatter induced by the variations due to the contour uncertainty. Rigorously, the results should be compared for larger numbers of independent data, but each sequence requires that the volunteer remains 15 min longer in the scanner, which is prohibitive. At least the comparison for two independent sets is promising. Two independent sets of data will also be acquired on the next volunteers in order to verify this tendency

4.5 Uncertainty

From the previous results, it seems that the main source of uncertainty is the error in defining the average contour of the artery. This error can be attributed to the poor spatial resolution of the MRI relatively to the size of the CCA. Indeed, the voxel size is at least of 0.4 mm. As the gradients are computed according to Eq. 5, it means that the

value of the gradient at one pixel is affected by the magnitude value of the preceding and following pixels. Thus the spatial resolution for tracking the contour is worse than 1 mm, which is very coarse knowing that the radius of the CCA is less than 5 mm. Moreover, averaging the magnitude over time for deducing the average contour is a supplementary effect that decreases the precision of contour detection. Therefore, the main source of uncertainty is the uncertainty about the location of the average contour curve $\overline{\mathfrak{C}}$.

Nevertheless, once the average contour curve is defined (manually or with the watershed algorithm), it has been shown that the deformations deduced by the optical flow method seems repeatable with negligible deviations, compared to the uncertainty induced by the definition of $\overline{\mathfrak{C}}$. This is rather promising.

Another source of uncertainty comes from the pressure measurements. Applanation tonometry has an accuracy of about less than 3% according to other studies [7]. Therefore, this remains small compared to the main source of uncertainty, that is the location of the average contour curve $\overline{\mathfrak{C}}$..

4.6 Consistency of the obtained material parameters

The modulus values reported in Tab. 2 are of correct range orders, as the elastic modulus of human arteries usually vary between 100 and 2000 kPa [21]. Our values are somewhat larger than the values from other studies about the CCA. Using a B-scan method, [22] found moduli of about 600 kPa on various patients. In [7], an echotracking method was used and a 3D, nonlinear, fiber-reinforced, hyperelastic, incompressible model of the wall was identified. The model includes residual stresses, smooth muscle tone, and perivascular tethering. The results shown in [7] prove that the stress/strain curve in the cyclic stress/strain range of the physiological conditions (corresponding to pressure variations of about $\pm$25 mmHg about the average blood pressure) is almost linear. Then, if one computes the equivalent Young modulus of the model presented in [7] , it is about 500 kPa on various patients. However, a significant role of the perivascular tissues was reported. This perivascular effect was considered separately, which tends to lower the identified elastic properties (see section 4.8).

In [22], it was shown that the obtained modulus values could have a standard deviation of about 250 kPa. This is almost twice larger than the standard deviations obtained by our method. This shows also that large variations can be expected from one individual to another.

V1 has a large blood pressure amplitude (75 mmHg) indicating arterial walls stiffer than common ones, which may explain the modulus larger than 1000 kPa.

All the pressure and deformation data are consistent. Especially, a good agreement with the segmentation (Fig. 7 and Fig. 9) is found, indicating that the stiffness values may be correct. The only uncertainty regards the thickness, which was not measured and chosen as 0.5 mm (a lot of measurements reported in the literature for the

CCA are around this value).

A lot of *in vitro* data are available in the literature. However, *in vitro* data provide the response of the tissue from zero stress up to failure, with generally an exponential shape. The elastic modulus corresponding to the physiological behaviour can be deduced from the slope of such *in vitro* curves by delimiting the maximum and minimum stress and strain between which the tissue remains *in vivo*. Such an approach for delimiting the physiological range was recently proposed and applied to the aorta by Duprey and coauthors [23]. We applied this approach to different *in vitro* stress/strain curves available for the CCA in the literature, like in [21, 24]. Results tend to show that the elastic modulus in the physiological range of stresses lies between 500 and 1000 kPa for the human CCA, which is well in agreement with the results reported here.

4.7 Comparison with other approaches

The advantage of the approach is that the deformation of the artery is measured across its whole cross section. This is a real advantage compared to ultrasound techniques [7] that only provide measurements of the radius. As the shape of the artery may not be round this is a significant advantage. This will be interesting when considering heterogeneous arteries such as the carotid artery with an atheromatous plaque. Here we focused on healthy arteries with thin walls for the first validation of the approach. But the potential of the approach is for thick walls with heterogeneities, where noninvasive elastographic techniques have to be developed for characterizing the mechanical properties of atherosclerotic plaques [9, 25].

Compared to classical segmentation, our approach has the advantage of having a subpixel accuracy.

4.8 Comparison with the Finite Element model

It was noted that the motion of the carotid artery is the combination of a translation towards the jugular vein and a uniform inflation (Fig. 5). The FE model was used to explain this effect. The values of the identified moduli were input in the FE code. A Poisson ratio of 0.49 was used for the artery and the surrounding medium. A value of E=20 kPa was used for the surrounding medium.

The FE model shows a similar distribution of the deformation all around the CCA, especially with largest deformations on the external part close to the jugular vein (Fig. 12).

Different models were set up in order to investigate the effect of the perivascular tissues on the behaviour of the carotid wall. It was noted that the response of the carotid to the intraluminal pressure is only affected marginally by the perivascular tissues: if the perivascular tissues are not considered, the response is modified by less than 10%. The effect of the mechanical properties of the jugular vein and of the fascia surrounding the carotid artery and the

jugular vein was also investigated. The wall of the jugular vein does not affect the response. The fascia does not change the motion of the carotid wall but it affects the deformation of the surrounding tissues. Outside the sheath made by the facia, the strain are very attenuated.

The objective of the model here was just to compare with the experimental data. More sophisticated model for the carotid artery, taking into account the bifurcation and fluid structure interactions with the blood, may be found in the literature

5 Conclusion

In conclusion, a new approach has been presented for time-resolved measurements of wall deformation in human arteries using MRI. The feasibility has been proved on an example. The purpose of the approach is to derive the local elastic properties of the carotid artery. Repeatable results obtained on two volunteers have pointed out the promising potential of this approach for investigating the mechanics of arterial tissues.

Applications are now envisaged on other arteries, like the aorta, for example in aneurisms or after stenting. Regarding the carotid artery, the approach will be applied to patients having atherosclerotic plaques in order to assess the stability of the plaques thanks to the measurement of deformations over a cardiac cycle.

Improvements of the approach are also under progress: accurate measurement of the average contour and of the thickness of the arterial wall, coupling possibly with an ultrasound technique [7]. Moreover, improvements of the MRI devices may also help to increase the spatial resolution of the technique for investigating small arteries like the internal carotid artery.

6 Acknowledgements

The authors would like to thank volunteers and staff. This study is part of the Imandef project (Grant ANR-08-JCJC-0071) funded by the ANR (French National Research Agency).

References

[1] J. Stalhand, A. Klarbring, and M. Karlsson. Towards in vivo aorta material identification and stress estimation. *Biomechanics and Modeling in Mechanobiology*, 2(3):169–186, 2004.

[2] C.A. Schulze-Bauer and G.A. Holzapfel. Determination of constitutive equations for human arteries from clinical data. *Journal of Biomechanics*, 36(2):165–169, 2003.

[3] R.W. Stadler, J.A. Taylor, and R.S. Lees. Comparison of B-mode, M-mode and echo-tracking methods for measurement of the arterial distension waveform. *Ultrasound in Medicine and Biology*, 23(6):879–887, 1997.

[4] V.R. Newey and D.K. Nassiri. Online artery diameter measurement in ultrasound images using artificial neural networks. *Ultrasound in Medicine and Biology*, 28(2):209–216, 2002.

[5] S.D. Kanters, O.E. Elgersma, J.D. Banga, M.S. Van Leeuwen, and A. Algra. Reproducibility of measurements of intima-media thickness and distensibility in the common carotid artery. *European Journal of Vascular and Endovascular Surgery*, 16(1):28–35, 1998.

[6] A.P. Hoeks, P.J. Brands, F.A. Smeets, and R.S. Reneman. Assessment of the distensibility of superficial arteries. *Ultrasound in Medicine and Biology*, 16(2):121–128, 1990.

[7] I. Masson, P. Boutouyrie, S. Laurent, J.D. Humphrey, and M. Zidi. Characterization of arterial wall mechanical behavior and stresses from human clinical data. *Journal of Biomechanics*, 41(12):2618–2627, 2008.

[8] K.V. Ramnarine, T. Hartshorne, Y. Sensier, M. Naylor, J. Walker, A.R. Naylor, R.B. Panerai, and D.H. Evans. Tissue doppler imaging of carotid plaque wall motion: a pilot study. *Cardiovascular Ultrasound*, 1:1–17, 2003.

[9] R.A. Baldewsing, C.L. De Korte, J.A. Schaar, F. Mastik, and A.F.W. Van Der Steen. Finite element modeling and intravascular ultrasound elastography of vulnerable plaques: parameter variation. *Ultrasonics*, 42:723–729, 2004.

[10] Z.-Y. Li, S. Howarth, R.A. Trivedi, J.M. U-King-Im, M.J. Graves, A. Brown, L. Wang, and J. Gillard. Stress analysis of carotid plaque rupture based on in vivo high resolution mri. *Journal of Biomechanics*, 39:2611–2622, 2006.

[11] M.R. Moreno, J.E. Moore, and R. Meuli. Cross-sectional deformation of the aorta as measured with magnetic resonance imaging. *Journal of Biomechanical Engineering, Transactions of the ASME*, 120:18–21, 1998.

[12] S. Avril, J.M. Huntley, and R. Cusack. In-vivo measurements of blood viscosity and wall stiffness in the carotid using PC-MRI. *European Journal of Computational Mechanics*, 18(1):9–20, 2009.

[13] C.C. Moore, E.R. McVeigh, and E.A. Zerhouni. Quantitative tagged magnetic resonance imaging of the normal human left ventricle. *Topics in Magnetic Resonance Imaging*, 11:359–371, 2000.

[14] M.T. Draney, R.J. Herfkens, T.J.R. Hugues, N.J. Pelc, K.L. Wedding, C.K. Zarins, and C.A. Taylor. Quantification of vessel wall cyclic strain using cine phase contrast magnetic resonance imaging. *Annals of Biomedical Engineering*, 30:1033–1045, 2002.

[15] J.P. Hornak. *The basics of MRI*. http://www.cis.rit.edu/htbooks/mri, 2007.

[16] D.W. MacRobbie, E.A. Moore, M.J. Graves, and M.R. Prince. *MRI: From Picture to Proton*. Cambridge University Press, 2003.

[17] Matlab®. http://www.mathworks.com, 2008.

[18] S.S. Beauchemin and J.L. Barron. *The computation of optical flow*. ACM New York, 1995.

[19] S. Avril, P. Feissel, F. Pierron, and Villon P. Comparison of two approaches for controlling the uncertainty in data differentiation: application to full-field measurements in solid mechanics. *Measurement Science and Technology*, 21(1):15703–15713, 2009.

[20] D. Shepard. A two-dimensional interpolation function for irregularly-spaced data. *Proceedings of the 1968 ACM National Conference*, pages 517–524, 1968.

[21] Y.C. Fung. *Biomechanics: Mechanical Properties of Living Tissues*. New York: Springer, 1993.

[22] R.H. Selzer, W.J. Mack, P.L. Lee, H. Kwong-Fu, and H.N. Hodis. Improved common carotid elasticity and intima-media thickness measurements from computer analysis of sequential ultrasound frames. *Atherosclerosis*, 154:185–193, 2001.

[23] A. Duprey, K. Khanafer, M. Schlicht, S. Avril, D. Williams, and R. Berguer. Ex vivo characterization of biomechanical behavior of ascending thoracic aortic aneurysm using uniaxial tensile testing. *European Journal of Vascular and Endovascular Surgery*, 2009. DOI: 10.1016/j.ejvs.2010.02.015.

[24] Z. Teng, D. Tang, J. Zheng, P.K. Woodard, and A.H. Hoffman. An experimental study on the ultimate strength of the adventitia and media of human atherosclerotic carotid arteries in circumferential and axial directions. *Journal of Biomechanics*, 42:2535–2539, 2009.

[25] S. Le Floc'h, J. Ohayon, P. Tracqui, G. Finet, A.M. Gharib, R.L. Maurice, G. Cloutier, and R.I. Pettigrew. Vulnerable atherosclerotic plaque elasticity reconstruction based on a segmentation-driven optimization procedure using strain measurements: theoretical framework. *IEEE Transactions on Medical Imaging*, 28(7).

List of Tables

parameter	V1 left	V1 right	V2 left	V2 right
identified value	837 kPa	1052 kPa	No result	896 kPa

Table 1: Obtained elastic moduli with the watershed segmented average contour.

parameter	V1 left	V1 right	V2 left	V2 right
identified value (average)	900 kPa	1008 kPa	755 kPa	819 kPa
standard deviation	47 kPa	98 kPa	78 kPa	52 kPa
coefficients of variation	5.3 %	9.8 %	100 %	6.3 %

Table 2: Obtained elastic moduli and variations when the contour is defined manually.

size of filtering kernel	R_x=R_y=0.3	R_x=R_y=0.6	R_x=R_y=0.9	R_x=R_y=1.2	R_x=R_y=1.5
identified value (average)	534 kPa	557 kPa	664 kPa	819 kPa	1000 kPa
standard deviation	50 kPa	55 kPa	60 kPa	52 kPa	70 kPa
coefficients of variation	9.4 %	10 %	9 %	6.3 %	7 %

Table 3: Obtained elastic moduli for the right carotid artery of V2 with different sizes of the filtering kernel R_x and R_y.

parameter	V1 left IRM1	V1 right IRM1	V1 left IRM2	V2 right IRM2
identified value (average)	1180 kPa	1340 kPa	1260 kPa	1330 kPa
standard deviation	63 kPa	131 kPa	60 kPa	180 kPa
coefficients of variation	5.3 %	9.8 %	100 %	14 %

Table 4: Comparison of the obtained elastic moduli obtained from two independent scans for the same volunteer.

List of Figures

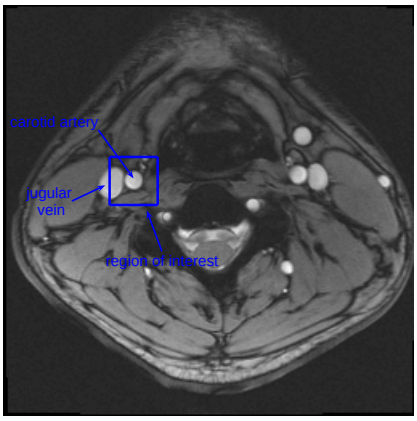

Figure 1: Example of magnitude image

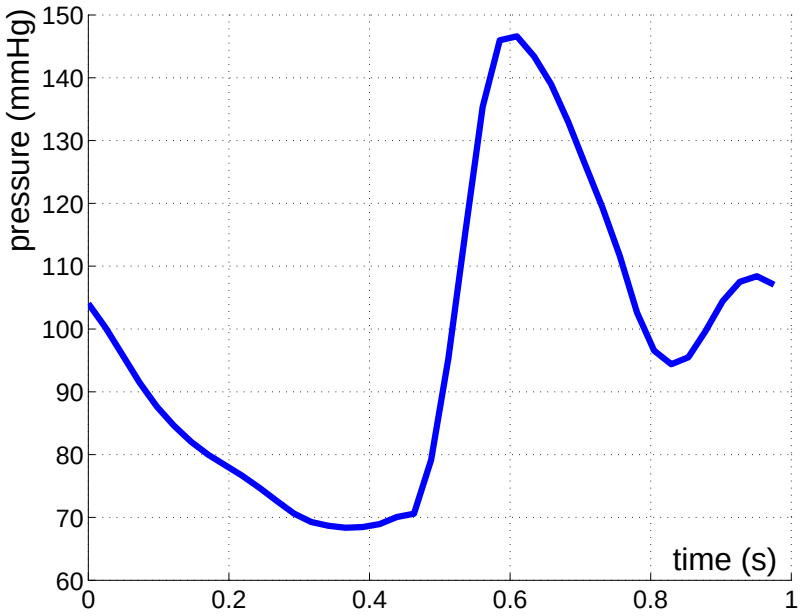

Figure 2: Example of pressure measurements

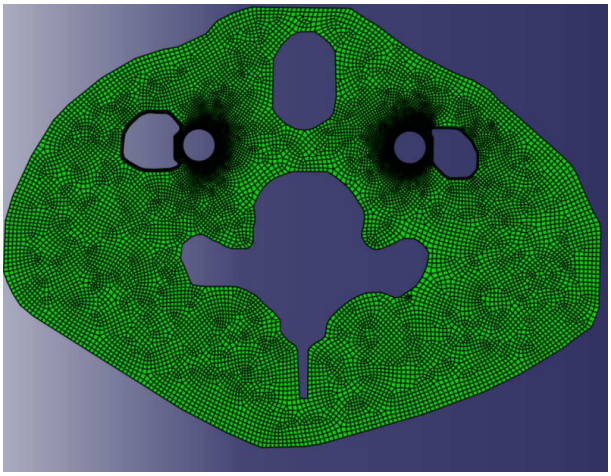

Figure 3: 2D mesh of the neck cross section.

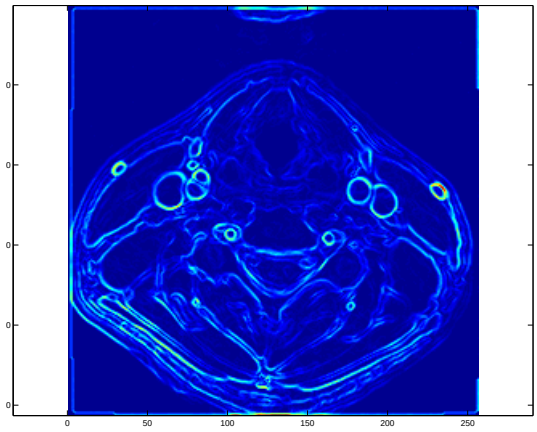

Figure 4: Example of gradient image

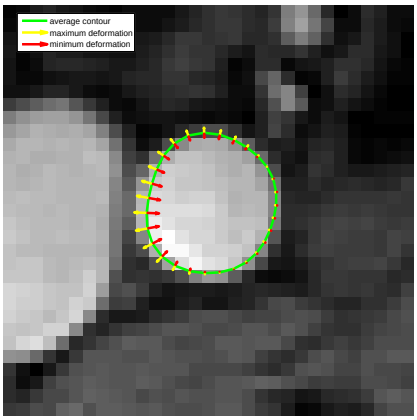

Figure 5: Maximum and minimum deformations measured for the CCA.

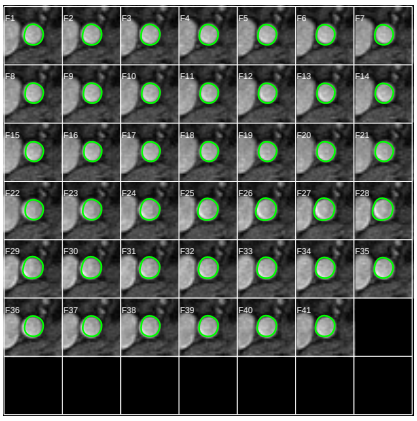

Figure 6: Contours of the CCA deformed using the deduced displacement values.

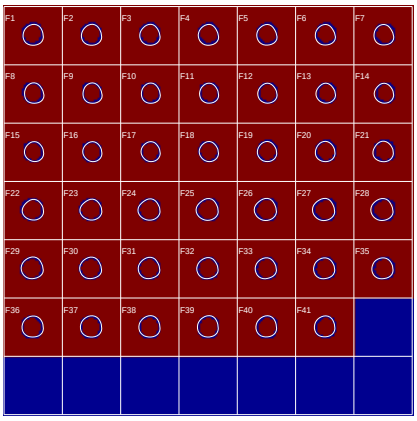

Figure 7: Comparison of contours obtained by segmentation of the magnitude or by updating an initial contour with the computed displacements.

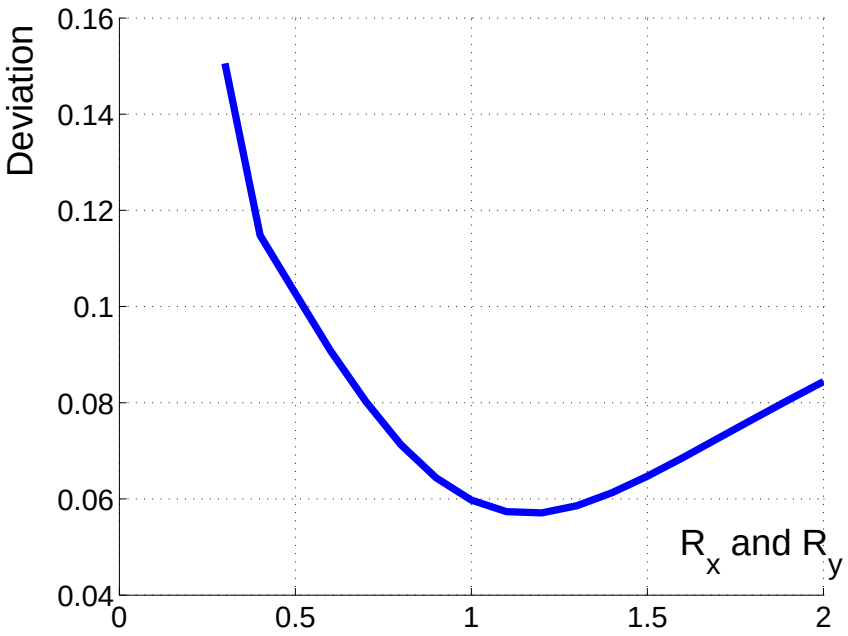

Figure 8: Effect of R_x and R_y on the contour detection.

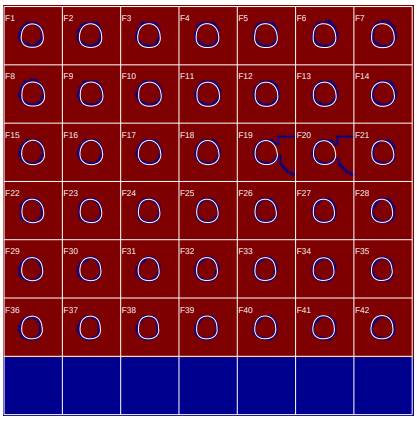

Figure 9: Comparison of contours obtained by segmentation of the magnitude or by updating an initial contour with the computed displacements. The segmentation failed for determining the contours at frame F19 and F20

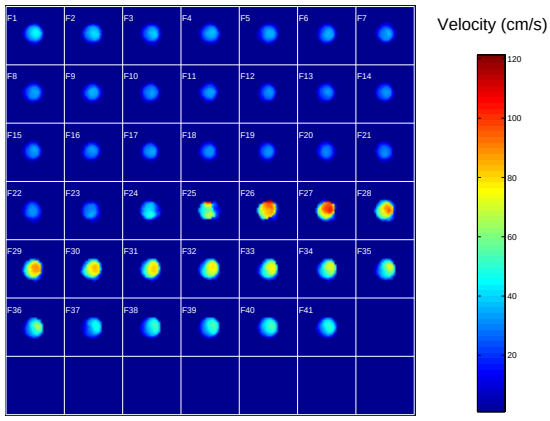

Figure 10: Velocity maps

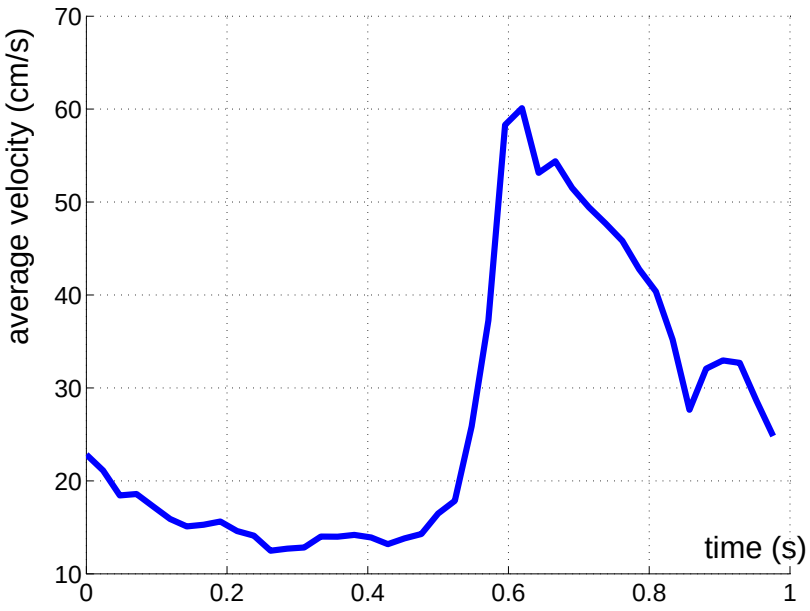

Figure 11: Variations of the average velocity over a cardiac cycle. The average velocity is assessed from the MRI data.

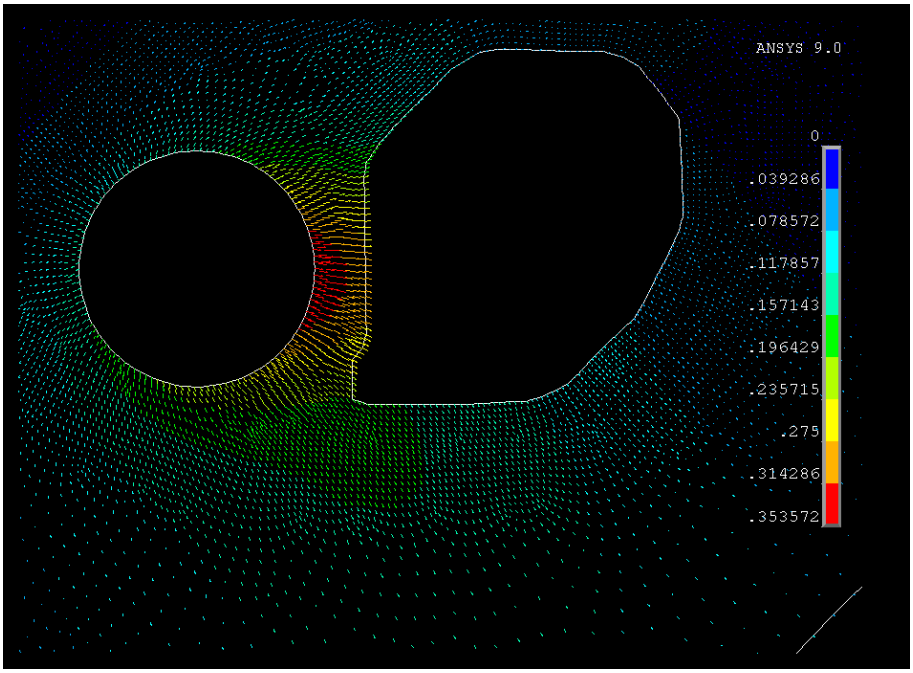

Figure 12: FE results zoomed around the carotid artery